Solid State Ionics 325 (2018) 80–89

Contents lists available at ScienceDirect

Solid State Ionics

journal homepage: www.elsevier.com/locate/ssi

Analysis of the statistical and convergence properties of ionic transport coefficients with application to the solid electrolyte Li_2OHCl

Jason David Howard, N.A.W. Holzwarth*

Department of Physics, Wake Forest University, Winston-Salem, NC 27109-7507, USA

ABSTRACT

The challenge of computing ionic transport coefficients from first principles is to achieve the necessary convergence with respect to system size, simulation time, and configurational sampling. Unfortunately current computer resources are not yet available for such convergence studies at the fully first principles level. In this work, a lattice kinetic Monte Carlo model is used to study the convergence properties of transport coefficients, using the Li sub-lattice of the Li ion electrolyte Li_2OHCl as an example system. The specific transport coefficients representing tracer diffusion, effective diffusion, and mobility are carefully studied for their convergence properties. Additionally, ion pair correlations of the effective diffusion are recast as a sum over events which allows for a detailed study of the nature of the correlation in terms of time and spatial separation. This experience suggests a general method of performing simulations by using first a kinetic Monte Carlo model followed by a first principles molecular dynamics study. For the Li_2OHCl system, the kinetic Monte Carlo results provide both a reference for the Haven ratio due to purely geometric effects and a measure of the computational effort needed to obtain meaningful molecular dynamics results. The combination of the two methods provides further evidence of anti-correlated Li-ion motion in this system as predicted in a previous study.

1. Introduction

Renewed technological interest in discovering crystalline solid electrolytes [1], has inspired the use of first principles computational methods for studying the properties of these materials, especially in simulating their ionic transport [2,3]. For ionic conductors whose conductivity mechanisms involve significant correlations among the mobile ions, it is computationally challenging to accurately simulate the transport properties. One such system that has received attention from several research efforts is Li_2OHCl and related compounds [4-8]. For this material in its disordered cubic phase, it has been suggested [7] that the mobile Li ions have correlated motion.

In fact, the notion of correlations affecting ionic conductivity is not new. Fifty years ago, the study of ionic conductivity for simple mechanisms and structures included corresponding estimates of correlation effects in terms of the Haven ratios [9-12]. More recently, the development of solid electrolyte materials for all-solid-state-battery technology has inspired new interest in accurate analysis and simulation of ionic conductivity with more complicated mechanisms and structures [13,14], for which the estimate of the Haven ratio is much more challenging. In order to gain insight into the convergence issues associated with evaluating ionic conductivity, we have analyzed an efficient and simple model based on a lattice kinetic Monte Carlo approach [15].

The remainder of the paper is organized as follows. The general formalism for evaluating ionic transport coefficients is reviewed in Section 2. The details of the lattice kinetic Monte Carlo method are presented in Section 3. The specific results of this work are based on the lattice structure appropriate to describing the disordered cubic phase of Li_2OHCl, but can be adapted to disordered lattice models more generally. Section 4 presents the detailed results of statistical and convergence properties of the lattice kinetic Monte Carlo simulations of the ionic transport parameters. In Section 5.1 the lattice kinetic Monte Carlo results are further analyzed in terms of temporal and spatial correlations. First principles simulations of this system are contrasted with the lattice kinetic Monte Carlo results in Section 5.2. Section 6 contains the summary and conclusions.

2. Formalism

There are several alternative methods of simulating ionic conductivity in solids [12]. For example, Kubo [16] showed that the fluctuation-dissipation theorem can be used in the absence of an explicit electrical field to evaluate transport properties of materials. The diagonal components of the conductivity tensor, $\sigma_{\alpha\alpha}$, (where α denotes the Cartesian components x, y, or z) is related to the time integral of the time auto correlation function of the current density $\mathbf{J}(t)$ vector components

$$\sigma_{\alpha\alpha}^{\mathrm{Kubo}} = \frac{V}{k_B T}\int_0^\infty \langle J_\alpha(t_0+\tau)J_\alpha(t_0)\rangle_{t_0} d\tau. \quad (1)$$

* Corresponding author.
E-mail address: natalie@wfu.edu (N.A.W. Holzwarth).

https://doi.org/10.1016/j.ssi.2018.07.025
Received 24 April 2018; Received in revised form 17 July 2018; Accepted 29 July 2018

In this expression, V represents the volume of the simulation cell, k_B is the Boltzmann constant, and T is the temperature. The $\langle\rangle_{t_0}$ brackets indicate ensemble averaging over initial configurations at time t_0 and the evaluation averages the $\alpha\alpha$ component of the conductivity tensor. For a system having ions of charge eQ_i and instantaneous particle velocities $\dot{\mathbf{R}}_i(t)$, the current density vector is given by

$$\mathbf{J}(t) = \frac{e}{V}\sum_{i=1}^{N} Q_i \dot{\mathbf{R}}_i(t), \tag{2}$$

where, in principle, the summation over particles i should include all ions in the simulation cell. However, in the following we will assume that it is a reasonable approximation that only the mobile ions need be included. We will further simplify the analysis to assume that there are N mobile ions within the simulation cell, each with the same charge $Q_i = Q$. With these approximations and by evaluating the time integral in Eq. (1), the diagonal conductivity tensor components can be expressed in terms of the instantaneous particle positions $\{\mathbf{R}_i(t)\}$ in the form [12,17]

$$\sigma_{\alpha\alpha}^{\text{Kubo}} = \frac{e^2}{2Vk_BT}\lim_{\tau\to\infty}\frac{1}{\tau}\langle p_\alpha(t_0,\tau)p_\alpha(t_0,\tau)\rangle_{t_0}, \tag{3}$$

expressed in terms of components of the charge moment vector which has the expression

$$\mathbf{p}(t_0,\tau) \equiv Q\sum_{i=1}^{N}(\delta\mathbf{R}_i(t_0,\tau)), \tag{4}$$

using the shorthand notation

$$\delta\mathbf{R}_i(t_0,\tau) \equiv \mathbf{R}_i(t_0+\tau) - \mathbf{R}_i(t_0). \tag{5}$$

In this work, we focus our attention on the diagonal x-components of the conductivity tensor. It is convenient to evaluate the square of the x-component of the moment vector as a sum of two types of contributions.

$$(p_x(t_0,\tau))^2 = Q^2(\Delta_{\text{sf}}(t_0,\tau) + \Delta_{\text{cr}}(t_0,\tau)), \tag{6}$$

Here the first "self-interaction" term includes the sum of the squares of the x-components of the displacements of each of the individual ions:

$$\Delta_{\text{sf}}(t_0,\tau) \equiv \Delta_{\text{sf}}^{x}(t_0,\tau) \equiv \sum_{i=1}^{N}(\delta X_i(t_0,\tau))^2. \tag{7}$$

The second "cross-interaction" term includes the sum of products of x-component displacements of all pairs of ions:

$$\Delta_{\text{cr}}(t_0,\tau) \equiv \Delta_{\text{cr}}^{x}(t_0,\tau) \equiv \sum_{i(\neq j)=1}^{N}\sum_{j=1}^{N}(\delta X_i(t_0,\tau)\delta X_j(t_0,\tau)). \tag{8}$$

The configuration average of the independent ion contribution $\langle\Delta_{\text{sf}}(t)\rangle_{t_0}$ determines the tracer diffusion coefficient D^{tracer} according to [12]

$$D^{\text{tracer}} = \lim_{\tau\to\infty} D^{\text{tracer}}(\tau), \quad \text{where}$$
$$D^{\text{tracer}}(\tau) \equiv \frac{1}{2N}\frac{1}{\tau}\langle\Delta_{\text{sf}}(t_0,\tau)\rangle_{t_0}. \tag{9}$$

Analogously, we can define a "cross" diffusion coefficient according to

$$D^{\text{cross}} = \lim_{\tau\to\infty} D^{\text{cross}}(\tau), \quad \text{where}$$
$$D^{\text{cross}}(\tau) \equiv \frac{1}{2N}\frac{1}{\tau}\langle\Delta_{\text{cr}}(t_0,\tau)\rangle_{t_0}. \tag{10}$$

The configuration average of the sum of "self" and "cross" interaction terms determines the effective diffusion coefficient according to [12]

$$D^{\text{effective}} = \lim_{\tau\to\infty} D^{\text{effective}}(\tau) \quad \text{where}$$
$$D^{\text{effective}}(\tau) \equiv D^{\text{tracer}}(\tau) + D^{\text{cross}}(\tau) \tag{11}$$

The ratio of the tracer and effective diffusion coefficients is known as the Haven ratio (H_r) [9-11,18] which provides a measure of the correlation of the conducting ions in terms of

$$\frac{1}{H_r} \equiv \frac{D^{\text{effective}}}{D^{\text{tracer}}} = 1 + \lim_{\tau\to\infty}\frac{\langle\Delta_{\text{cr}}(t_0,\tau)\rangle_{t_0}}{\langle\Delta_{\text{sf}}(t_0,\tau)\rangle_{t_0}}. \tag{12}$$

The diffusion coefficients are related to diagonal components of the ionic conductivity tensor through the Nernst-Einstein relationship as well as following from the Kubo formalism of Eq. (1):

$$\sigma_{xx}^{\text{Kubo}} = \frac{N}{V}\frac{e^2Q^2D^{\text{effective}}}{k_BT} = \frac{N}{V}\frac{e^2Q^2D^{\text{tracer}}}{k_BTH_r}. \tag{13}$$

An alternative analysis of ionic conductivity follows from the inverse Ohm's law as the response of the time averaged current density in the α direction to an electric field F_α.

$$\langle J_\alpha(t)\rangle_t = \sigma_{\alpha\alpha}^{\text{Ohm}}F_\alpha. \tag{14}$$

Using Eq. (2) in the presence of an electric field in the x-direction within the linear response regime, the Ohmic conductivity can be estimated from

$$\sigma_{xx}^{\text{Ohm}} = \frac{eQN}{V}\langle\mu_x(t_0)\rangle_{t_0}, \tag{15}$$

where the ion mobility for a given initial configurations $\{\mathbf{R}_i(t_0)\}$ is given by

$$\mu_x(t_0) \equiv \lim_{F_x\to 0}\left(\frac{1}{F_x}\lim_{\tau\to\infty}\left(\frac{1}{\tau}\left(\frac{1}{N}\sum_{i=1}^{N}\delta X_i^{F_x}(t_0,\tau)\right)\right)\right). \tag{16}$$

Here the F_x superscript on the ion displacement is used to indicate the field dependence of the trajectory for this case. The corresponding effective diffusion coefficient associated with the ion mobility can be defined by

$$D_\mu^{\text{effective}} = \frac{k_BT\langle\mu_x(t_0)\rangle_{t_0}}{eQ}. \tag{17}$$

In order to accurately simulate ionic conductivity for a system using Eqs. (13) or (15), several numerical and physical approximations must be made. At the present time, the "state of the art" for simulating ionic conductivity [3,7,8,13,14] uses first-principles methods to evaluate forces between ions. However, while the physics of the particle interactions is well represented, convergence of the results with respect to simulation size and time may not be as well under control. In this work we focus on these convergence issues for a simplified model of the ionic forces.

3. Calculational details

In order to efficiently evaluate the expressions discussed in Section 2, we used a lattice based kinetic Monte Carlo approach [19-21]. The N mobile ion positions $\{\mathbf{R}_i(t)\}$ are calculated within a supercell lattice having N_T available sites, each with an average occupancy of $o = N/N_T < 1$ and each with ν nearest neighbor sites, at a series of "times" t_s. Here, we enumerate the steps $s = 1,2,...S$ with fixed time intervals $\delta\tau$ according to

$$t_s = t_0 + s\delta\tau. \tag{18}$$

Here, $\delta\tau$ is an arbitrary time increment which does not affect the simulation. It can be related to a physical time with additional model considerations. The Monte Carlo algorithm used in this work is as follows.

1. At the initial time t_0, the sites are occupied using a random number generator to produce $\{\mathbf{R}_i(t_0)\}$.
2. For subsequent time steps, $s \geq 1$, the following procedure updates the positions to $\{\mathbf{R}_i(t_s)\}$.

(a) A random number generator chooses one of the occupied sites $1 \le j \le N$.
(b) A random number generator chooses a nearest neighbor to $\mathbf{R}_j(t_{s-1})$ among the ν possible choices.
(c) If the chosen nearest neighbor is unoccupied, then site $\mathbf{R}_j(t_{s-1})$ is moved to that site to form a new position $\mathbf{R}_j(t_s)$ and the configuration is updated accordingly to form $\{\mathbf{R}_i(t_s)\}$.
(d) Otherwise the configuration $\{\mathbf{R}_i(t_s)\}$ remains the same as for the previous time step.

Some practical details are noted as follows.

3. The algorithm can be modified on Step #2(c) by introducing an activation energy E_A so that for a system temperature of T, the update of $\mathbf{R}_j(t_s)$ the chosen and available site is made with a probability $\exp(-E_A/(k_BT))$.
4. Assuming ergodicity in the simulation, the data in the simulation can be used for analyzing multiple time sequences by shifting configurations at time t_s to the initial time t_0 by setting $\{\mathbf{R}_i(t_s)\} \rightarrow \{\mathbf{R}_i(t_0)\}$.
5. In order to relate the results for various simulation times and supercell sizes, the time counter s is related to a scaled time counter $\bar{s}$ as the average number of hops per ion in the simulation. While the time counter s is used within each simulation, the results are reported in terms of the scaled time counter $\bar{s}$. Explicitly, the scaled time counter is defined according to

$$\bar{s} = \frac{s(1-o)}{N} e^{-E_A/kT}. \tag{19}$$

For this simple model [22], the activation energy E_A is isotropic and configuration independent and therefore the temperature does not contribute to the statistical and convergence properties of the simulations. In practice, simulations in the absence of a biasing electric field $\mathbf{F}$ are carried out in the limit of infinite temperature.
6. In order to model the mobility in the presence of an electric field $\mathbf{F}$ according to Eq. (15), the algorithm must be modified in the following way [20]. On a given time step t_s for Step #2c involving ion j, for a possible hop from nearest neighbor sites $\mathbf{R}_j(t_{s-1})$ to $\mathbf{R}_j(t_s)$, it is assumed that the activation energy E_A is modified by

$$\epsilon \equiv -\frac{1}{2} eQ\mathbf{F}\cdot(\mathbf{R}_j(t_s) - \mathbf{R}_j(t_{s-1})). \tag{20}$$

The definition of ϵ is such that for $Q > 0$, when the hop is along the field, the activation energy is slightly lowered. Now the update of $\mathbf{R}_j(t_s)$ is made with a probability $\exp(-(E_A+\epsilon)/(k_BT))$; otherwise the ion position is kept at its earlier position $\mathbf{R}_j(t_s) = \mathbf{R}_j(t_{s-1})$. In practice, the values were chosen such that $\epsilon/(k_BT) = 0.04$ and $E_A/(k_BT) = 1.45$ so that the linear approximation

$$e^{-(E_A-\epsilon)/(k_BT)} - e^{-(E_A+\epsilon)/(k_BT)} \approx \frac{2\epsilon}{k_BT} e^{-E_A/(k_BT)}, \tag{21}$$

was sufficiently accurate and the Monte Carlo acceptance rate was efficient.

The lattice for this study is based on the Li sites available for the disordered cubic phase of Li_2OHCl which is a member of a family of promising solid electrolytes recently studied by our group and others [4-8], as shown in Fig. 1. The three unique lattice sites within the cubic unit cell are listed in the figure caption. In this case, each site has a probability of occupancy of $o = \frac{2}{3}$ and has 8 nearest-neighbors ($\nu = 8$). Missing from this model are the effects of the Cl^- ion located at fractional coordinate $\left(\frac{1}{2}, \frac{1}{2}, \frac{1}{2}\right)$ and the effects of O located at the origin and associated with an OH^- ion. In practice, scaled units are used to measure displacement and time.

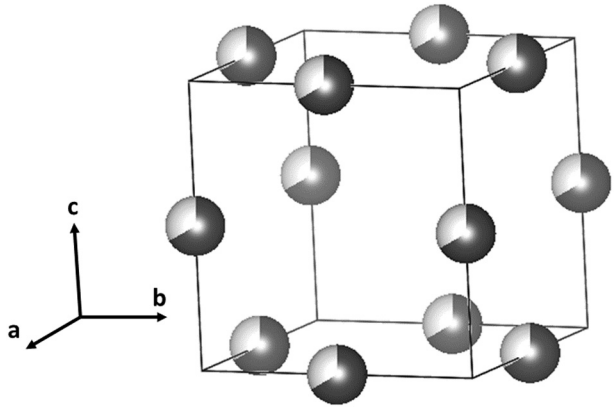

Fig. 1. Cubic unit cell for simulations in this study with the origin at lower back left corner is shown together with available Li sites indicated with two-thirds shaded volumes corresponding to their average occupancy. The fractional coordinates of the unique sites are Li(1) at $\left(\frac{1}{2}, 0, 0\right)$, Li(2) at $\left(0, \frac{1}{2}, 0\right)$, and Li(3) at $\left(0, 0, \frac{1}{2}\right)$.

$$\delta X_i(t_0, \tau) \rightarrow \delta X_i(t_0, \bar{s})/(a/2) \equiv \delta X_i(t_0, \bar{s}), \tag{22}$$

where $a/2$ is the hop length along the x-axis for a cubic unit cell of lattice constant a. For convenience, a was taken to be 2 within the Monte Carlo simulations. In the remainder of this paper, all diffusion constants are given in units of the square of the one-dimensional hop length per hop/ion.

4. Results

4.1. Statistical analysis of Monte Carlo simulations

There are several competing variables which effect the simulation results, including configuration sampling, number of simulation steps, and sample size. Because of the computational accessibility of the model, we can study each of these separately.

First we consider effects of the initial configurations $\{\mathbf{R}_i(t_0)\}$. In order to illustrate the sensitivity of the "self" $\Delta_{sf}(t_0, \bar{s})$ and "cross" $\Delta_{cr}(t_0, \bar{s})$ terms to the initial configurations, examples are shown in Fig. 2. These examples were generated using supercells of size $12 \times 12 \times 12$ units ($N = 3456$) for two different initial configurations

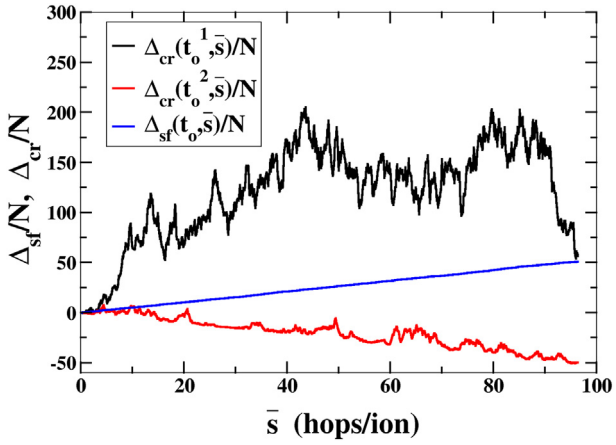

Fig. 2. Comparison of the squared displacement results for a supercell composed of $12 \times 12 \times 12$ units and two initial configurations $\{\mathbf{R}_i(t_0^1)\}$ and $\{\mathbf{R}_i(t_0^2)\}$. Plots illustrate the "self" term $\Delta_{sf}(t_0^l, \bar{s})/N$ and "cross" term $\Delta_{cr}(t_0^l, \bar{s})/N$ ($l = 1,2$) contributions as functions of the scaled step counter $\bar{s}$. For the samples shown, the curves for $\Delta_{sf}(t_0^1, \bar{s})/N$ and $\Delta_{sf}(t_0^2, \bar{s})/N$ coincide, while the curves for $\Delta_{cr}(t_0^1, \bar{s})/N$ and $\Delta_{cr}(t_0^2, \bar{s})/N$ illustrate two extremes.

$\{\mathbf{R}_i(t_0^l)\}$, plotted as a function of the scaled step counter $\bar{s}$. From this plot it is apparent that both initial configurations give the same result for $\Delta_{sf}(t_0^l, \bar{s})$ which tends to increase monotonically with time. By contrast, the $\Delta_{cr}(t_0, \bar{s})$ term varies widely as a function of the step counter $\bar{s}$ and very differently for the two different initial configurations. In order to highlight its sensitive behavior, the plots of $\Delta_{cr}(t_0, \bar{s})$ shown in Fig. 2 illustrate some of the extreme variations. For $\Delta_{cr}(t_0^1, \bar{s})$, the values are generally positive, while for $\Delta_{cr}(t_0^2, \bar{s})$ the values are generally negative.

In order to take advantage of statistical analyses of a general result Y_l from this study, it will be convenient to define a mean value and standard deviation according to [23]

$$\left\langle Y \right\rangle \equiv M_Y \equiv \frac{1}{L}\sum_{l=1}^{L} Y_l \quad \text{and} \quad \Sigma_Y \equiv \sqrt{\frac{1}{L}\sum_{l=1}^{L}(Y_l - M_Y)^2}, \tag{23}$$

where L denotes the number of samples. From these values, it is often of practical interest to estimate the number of samples L_f needed to to ensure a fractional error of f. Assuming that the fractional error is well estimated by the ratio of the standard deviation of the mean to the mean value, we can infer that

$$L_f \approx \left(\frac{\Sigma_Y/M_Y}{f}\right)^2, \tag{24}$$

which follows from the statistical relationship [23]$\Sigma_{M_Y} = \Sigma_Y/\sqrt{L_f}$.

In order to visualize the statistical properties of the squared displacement functions, it is useful to consider histogram plots of their distributions. The simulations were carried out for a supercell composed of 12 × 12 × 12 units (N = 3456) fixing the time interval of the simulation corresponding to $\bar{s}$ = 15 hops/ion. These distributions were generated from $L = 8 \times 10^5$ samples of the initial configurations $\{\mathbf{R}_i(t_0^l)\}$. Figs. 3 and 4 show histograms of $\Delta_{sf}(t_0^l, \bar{s})/(2N\bar{s})$ and $\Delta_{cr}(t_0^l, \bar{s})/(2N\bar{s})$, respectively. These plots show that the distribution for Δ_{sf} has a Gaussian like shape, while the distribution for Δ_{cr} is highly asymmetric. While not presented in a plot, we find that the histogram plot for the corresponding ion mobility $\mu_x(t_0^l)$ given by Eq. (16) also has a Gaussian shaped distribution.

The probability distribution for $Y_l = \Delta_{sf}(t_0^l, \bar{s})/(2N\bar{s})$ is highly localized with Gaussian shape with a mean value of $M_Y = 0.275$ and standard deviation of $\Sigma_Y = 0.007$. The probability distribution for $Y_l = \Delta_{cr}(t_0^l, \bar{s})/(2N\bar{s})$ shows a very asymmetric distribution with average value of $M_Y = 0.055$ and a large standard deviation of $\Sigma_Y = 0.452$. It is apparent from the shape of this probability distribution, that the difficulty in converging $\Delta_{cr}(t_0, \bar{s})$ comes from the non-trivial number of large value contributions. While the probability density of these large value contributions is small, their contribution is significant. The range of values of Δ_{cr} can be estimated as follows. At the lower bound,

$$\Delta_{cr} \geq -\Delta_{sf}, \tag{25}$$

which follows from the fact that the sum of $\Delta_{sf} + \Delta_{cr} \geq 0$, because of its proportionality to the squared length of the moment component p_x as defined in Eq. (6). The upper bound can be estimated from the value obtained when all of the hops are in the same direction which would result in the very rare upper bound value of

$$\Delta_{cr} \leq N(N-1)\bar{s}^2. \tag{26}$$

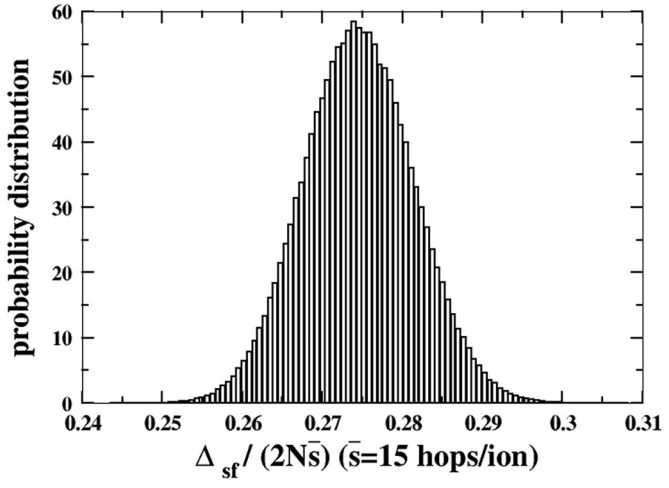

Fig. 3. Distribution of values of $\Delta_{sf}(t_0, \bar{s})/(2N\bar{s})$ at a fixed time interval $\bar{s}$ corresponding to $\bar{s}$ = 15 hops/ion for a 12 × 12 × 12 supercell (N = 3456). The probability distribution was constructed with 8×10^5 initial configurations and normalized to unity.

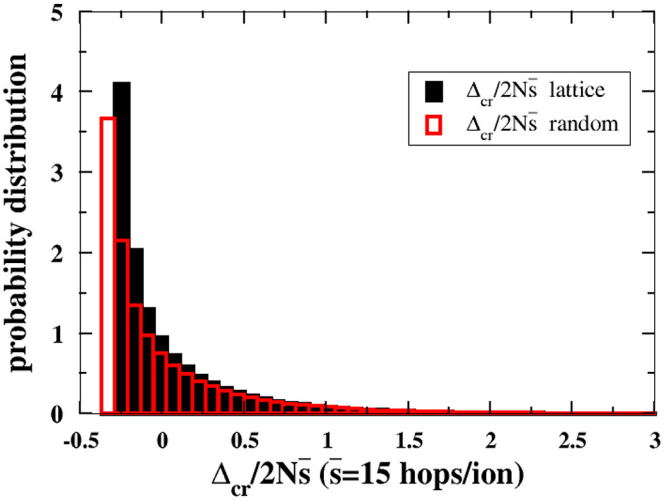

Fig. 4. Distribution of values of $\Delta_{cr}(t_0, \bar{s})/(2N\bar{s})$ at a fixed interval $\bar{s}$ corresponding to $\bar{s}$ = 15 hops/ion for 12 × 12 × 12 supercell (N = 3456). The probability distribution was constructed with 8×10^5 initial configurations and normalized to unity presented with filled black bars. The equivalent distribution for a one-dimensional random walk is represented with red-outlined bars for comparison.

To better understand the shapes of the probability curves for the self and cross correlation terms, it is useful to consider the analogous quantities that can be derived from a one-dimensional random walk. The trajectories of N independent random walkers $\{X_i^{RW}(t_s)\}$ can be used to compute $\Delta_{sf}{}^{RW}$ and $\Delta_{cr}{}^{RW}$ according to Eqs. (7) and (8), respectively. In order to ensure correspondence with our cubic model with $\bar{s}$ = 15 hops per ion, the random walk simulations were performed for 10 steps, representing two-thirds of the hops along the x-axis. In calculating these numbers, care was taken to make sure that their scaling is consistent with the corresponding cubic lattice model. The normalized probability distribution is presented in Fig. 4. For this one-dimensional random walk, with $Y = \Delta_{cr}^{RW}/(2N\bar{s})$, the mean value and standard deviations are given by $M_Y = -4 \times 10^{-5}$ and $\Sigma_Y = 0.470$. The corresponding self term $Y = \Delta_{sf}^{RW}/(2N\bar{s})$ for this random walk has the mean value and standard deviation of $M_Y = 0.333$ and $\Sigma_Y = 0.008$, respectively. The numerical values for this one-dimensional random walk system are consistent with the textbook results. They differ from our three-dimensional cubic model system reflecting the effects of geometry and the effects of particle interactions due to site occupations.

Another important consideration is the behavior of the standard deviations of Δ_{sf}, Δ_{cr} and μ_x as a function of simulation size. We have considered supercell sizes of $n \times n \times n$ multiples of the unit cell for $2 \leq n \leq 16$. The ratios of standard deviations to mean values of Δ_{sf}, Δ_{cr} and μ_x are given in Fig. 5. These calculations were all performed at a fixed value of the effective hops $\bar{s}$ and are all well converged with respect to the number of initial configurations $\{\mathbf{R}_i(t_0^l)\}$. These plots show that the $\Sigma_Y/\langle Y \rangle$ ratios converge to 0 with increasing simulation cell size for both Δ_{sf} and μ_x. However, for Δ_{cr}, the $\Sigma_Y/\langle Y \rangle$ ratio seems to asymptote to a non-zero value for very large simulation cell sizes.

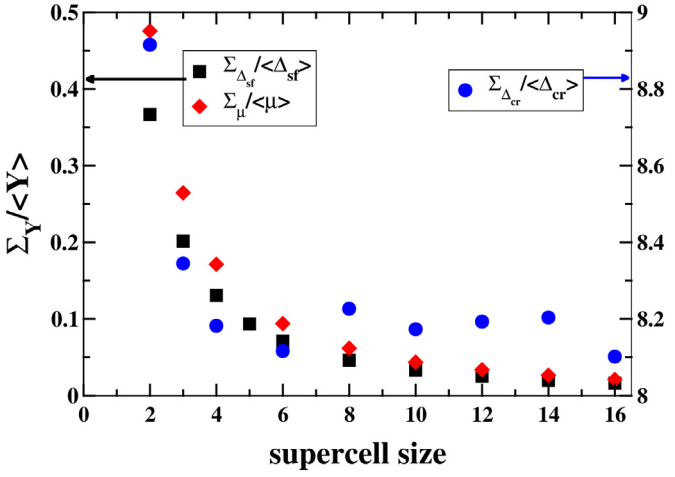

Fig. 5. Ratios of standard deviations to mean values of Δ_{sf} and μ_x (left scale) and Δ_{cr} (right scale) as a function of the supercell size parameter n. For Δ_{sf} and Δ_{cr}, the calculations were performed at $\bar{s} = 15$ hops/ion. For μ_x the calculations were performed with 6 hops/ion on average along the field direction, corresponding approximately to $\bar{s} = 880$ hops/ion. The parameters $E_A/(k_BT)$ and $\epsilon/(k_BT)$ were taken as described in Section 3.

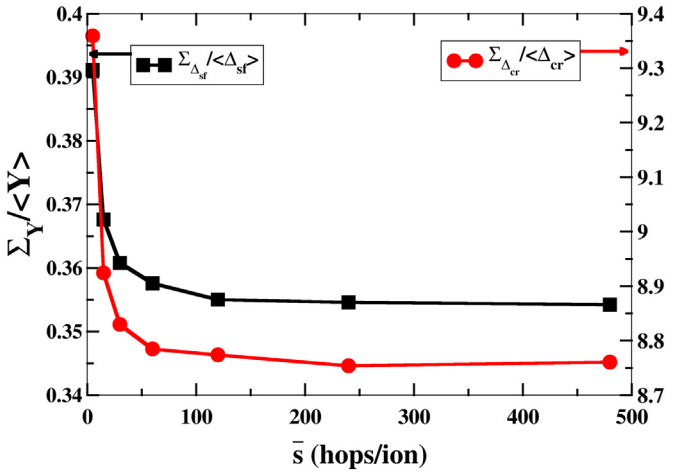

Fig. 6. Values of $\Sigma_Y/\langle Y\rangle$ for $Y = \Delta_{sf}$ (left scale) and for $Y = \Delta_{cr}$ (right scale) as a function of $\bar{s}$ for very long simulations. Simulations were performed in $2 \times 2 \times 2$ supercells ($N = 16$).

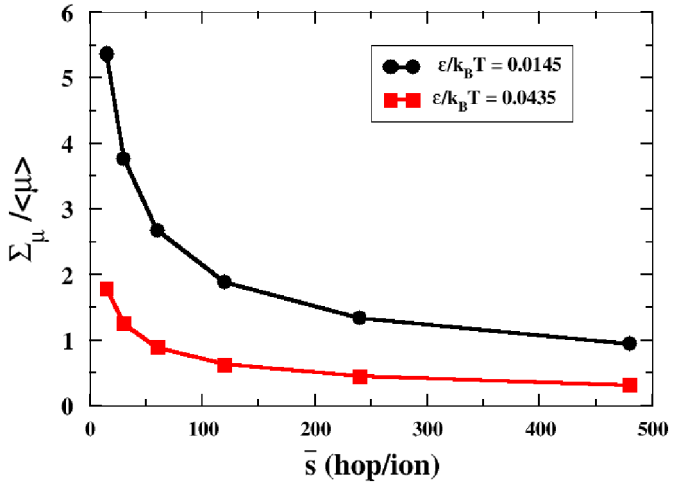

Fig. 7. Values of $\Sigma_Y/\langle Y\rangle$ for $Y = \mu_x$ as a function of $\bar{s}$ for very long simulations performed for $2 \times 2 \times 2$ supercells ($N = 16$). Results for two different values of field strength as measured by $\epsilon/(k_BT)$ are presented. For both cases the same activation energy of $E_A/(k_BT) = 1.45$ was used.

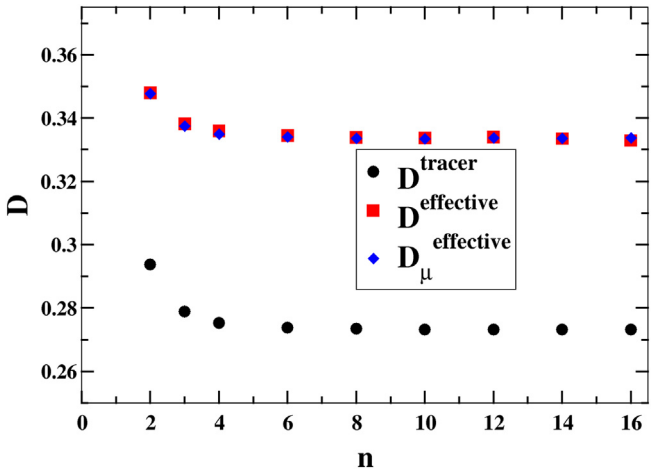

Fig. 8. Comparison of diffusion constants D^{tracer}, $D^{effective}$, and $D_\mu^{effective}$ calculated using Eqs. (9), (11), and (17), respectively as a function n representing the supercell multiplicity of $n \times n \times n$. All calculations were performed in the $\bar{s} \to \infty$ limit and are also well converged with respect to initial configurations $\{\mathbf{R}_i(t_0)\}$.

Finally we consider the behavior of the standard deviations of Δ_{sf}, Δ_{cr} and μ_x as a function of simulation time as measured by the scaled parameter $\bar{s}$. In order to carry out very long simulations, we consider small supercells composed of $2 \times 2 \times 2$ units with $0 < \bar{s} < 500$. Fig. 6 shows that the ratio of $\Sigma_Y/\langle Y\rangle$ for $Y = \Delta_{cr}$ asymptotes to a value which is more than 20 times larger than that of $Y = \Delta_{sf}$. According to Eq. (24), this means that more than 400 times as many samples are needed to converge Δ_{cr} compared with Δ_{sf}.

We also examined the convergence of the standard deviation in simulating the mobility at different electric field strengths as shown in Fig. 7. This plot shows that the standard deviation ratio asymptotes to zero for $\bar{s} \to \infty$, although a larger field strength (within the linear range) converges more rapidly.

4.2. Convergence of the transport coefficients

For evaluating the diffusion constants D^{tracer}, $D^{effective}$, and $D_\mu^{effective}$, it is necessary to carry out the simulations in the $\bar{s} \to \infty$ limit. These quantities are shown in Fig. 8 as a function of simulation cell size. Results also show that the results calculated using the Kubo formalism and using the Ohm's law formalism are in very good agreement. The standard deviation of the results due to the averaging over initial configurations $\{\mathbf{R}_i(t_0)\}$ is too small to be seen on this scale.

In order to see the results in a little more detail, Fig. 9 shows the Haven ratio as defined in Eq. (12) as a function of simulation cell size. These results show that very good convergence at a value of $H_r = 0.819$ is achieved for a supercell size of $6 \times 6 \times 6$. On this scale, the error bars (representing the standard deviation of the mean) are visible, but small for both the Kubo and Ohm's law simulations.

Finally, in Fig. 10, a more realistic estimate of the time convergence of the diffusion constant is presented for simulations on $6 \times 6 \times 6$ unit supercells. These calculations were performed on a very large number of initial configurations so that the values are converged with their standard deviation of the mean values smaller than the line width of the plot. For these highly sampled simulations, the time convergence of D^{tracer} mirrors that of D^{cross} such that their time convergence for the individual terms is seen to be quite good at $\bar{s} = 2$ hops/ion. Interestingly, the total diffusion $D^{effective}$ converges at short times for this model.

For the highly sampled simulations in cubic simulation cells, the

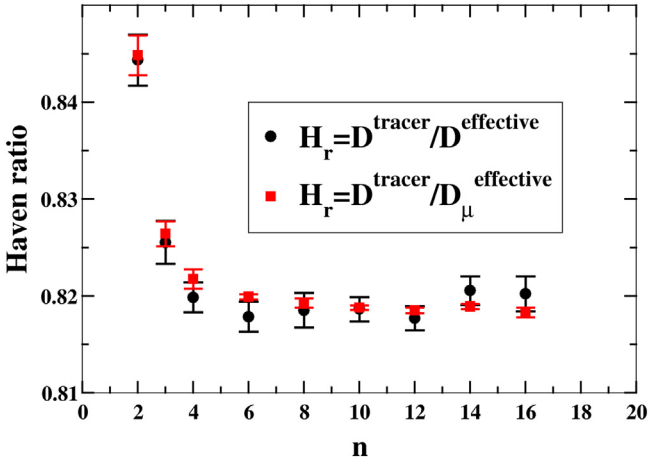

Fig. 9. Simulated values of the Haven ratio H_r as defined by Eq. (12) as a function of the simulation cell parameter n, comparing results calculated using the Kubo (black circles) and Ohm's law (red squares) methods. The error bars on the graph indicate the standard deviation of the mean of the value. The calculations were performed with $\bar{s} \to \infty$ and a large number of initial configurations.

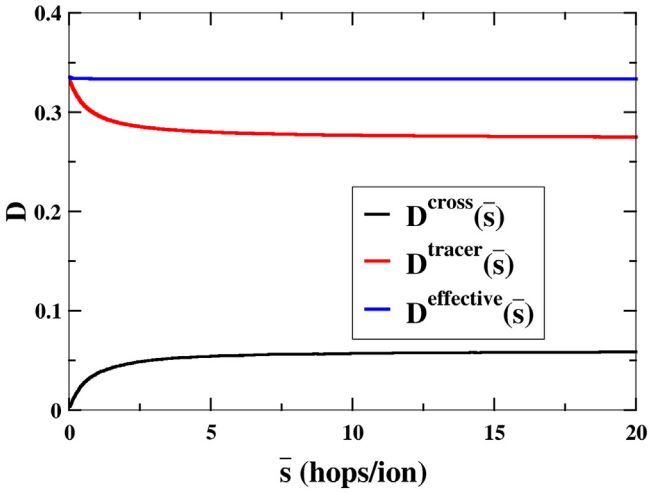

Fig. 10. Convergence of $D^{\text{effective}}(\bar{s})$, $D^{\text{tracer}}(\bar{s})$ and $D^{\text{cross}}(\bar{s})$ as defined in Eqs. (11), (9) and (10), before taking the asymptotic limit, as a function of $\bar{s}$. Simulations were performed on a 6 × 6 × 6 supercell.

time convergence of the diffusion coefficients can be well interpolated by a simple analytic form based on a single exponential:

$$D^{\text{cross}}_{\text{model}}(\bar{s}) \approx D_\infty e^{-w/\bar{s}}, \tag{27}$$

where D_∞ and w are fitting parameters. For the 6 × 6 × 6 supercell shown in Fig. 10. Some typical values of the fitting parameters are given in Table 1. For asymmetric simulation cells, it is found that typically more than one exponential function is needed to achieve an accurate fit.

Table 1
Values of fitting parameters defined in Eq. (27) used for diffusion coefficients simulated with the kinetic Monte Carlo model for $n \times n \times n$ supercells.

n	D_∞	w
2	0.054	0.344
6	0.060	0.472

5. Analysis

5.1. Properties of the cross particle displacement contributions

The simulations presented in Section 4.1 document how sensitive the calculations are to the cross particle contributions given by $\Delta_{\text{cr}}(t_0,\tau)$ as defined in Eq. (8). In this section, the term is analyzed further in order to detail its properties. An important point to make about Eq. (8) is that for a collection of truly random and independent hoping events, the ensemble average $\langle \delta X_i(t_0,\tau)\delta X_j(t_0,\tau)\rangle_{t_0}$ is equal to zero. Consequently, the extent to which $\langle \Delta_{\text{cr}}(t_0,\tau)\rangle_{t_0}$ differs from zero is a measure of correlations in the system. Ideally, one could reformulate Eq. (8) into correlated contributions to include in the evaluation in such a way that they well approximate $\langle \Delta_{\text{cr}}(t_0,\tau)\rangle_{t_0}$. Denoting this correlated cross particle displacement contribution by $\langle \Delta^{\text{corr}}_{\text{cr}}(t_0,\tau)\rangle_{t_0}$, we expect that it should well approximate the full contribution in the sense that

$$|\langle \Delta^{\text{corr}}_{\text{cr}}(t_0,\tau)\rangle_{t_0} - \langle \Delta_{\text{cr}}(t_0,\tau)\rangle_{t_0}| < \epsilon. \tag{28}$$

where ϵ is some small number within the desired convergence criteria.

In order formulate the correlated contributions, we first partition the particle displacement defined in Eq. (5) into a sum over sequential displacements. For displacement along the x-axis, we define a displacement "event" $\Lambda_{i\lambda}(t_0)$ such that

$$\delta X_i(t_0,\tau) \equiv X_i(t_0+\tau) - X_i(t_0) = \sum_{\lambda=1}^{\hat{s}} \Lambda_{i\lambda}(t_0). \tag{29}$$

Here λ is an index for the time sequence similar to that defined in Eq. (18)

$$t_\lambda = t_0 + \lambda\delta\hat{\tau}, \tag{30}$$

where it is computationally efficient to define the time increment $\delta\hat{\tau}$ to be an integer multiple of $\delta\tau$ used in simulation so that $\delta\hat{\tau} > \delta\tau$. In this work, a $\delta\hat{\tau}$ equivalent to the incremental scaled step counter $\Delta\bar{s}$=0.25 hops/ion was used. The displacement event for particle i is then defined according to

$$\Lambda_{i\lambda}(t_0) \equiv X_i(t_0+\lambda\delta\hat{\tau}) - X_i(t_0+(\lambda-1)\delta\hat{\tau}). \tag{31}$$

Accordingly, the maximum step counter, $\hat{s}$, for the coarse grained evaluation is chosen such that $\hat{s}\delta\hat{\tau} = \tau$. Now the cross interaction term of Eq. (8) can be equivalently rewritten in the form

$$\Delta_{\text{cr}}(t_0,\tau) = \sum_{i(\neq j)=1}^{N}\sum_{j=1}^{N}\sum_{\lambda=1}^{\hat{s}}\sum_{\lambda'=1}^{\hat{s}} (\Lambda_{i\lambda}(t_0)\Lambda_{j\lambda'}(t_0)). \tag{32}$$

In this formulation, the idea is to choose from all of the cross event products $\Lambda_{i\lambda}(t_0)\Lambda_{j\lambda'}(t_0)$, only those which are "correlated". The expectation is that the correlation is limited in time and space, so that it should be possible to choose cutoff parameters t_{cut} and R_{cut} to limit the full summation in Eq. (32) in the form

$$\Delta^{\text{corr}}_{\text{cr}}\left(t_0,\tau\right) = \sum_{i(\neq j)=1}^{N}\sum_{j=1}^{N}\sum_{\lambda=1}^{\hat{s}}\sum_{\lambda'=1}^{\hat{s}} (\Lambda_{i\lambda}(t_0)\Lambda_{j\lambda'}(t_0)) f_{ij\lambda\lambda'}\left(t_{\text{cut}}, R_{\text{cut}}\right), \tag{33}$$

where $f_{ij\lambda\lambda'}(t_{\text{cut}}, R_{\text{cut}})$, represents a function designed to model the correlations of the system. For example, a simple functional form can be written in terms of the Heaviside step functions $\Theta(x)$,

$$f_{ij\lambda\lambda'}(t_{\text{cut}}, R_{\text{cut}}) \equiv \Theta(t_{\text{cut}} - |\lambda'-\lambda|\delta\hat{\tau})\,\Theta(R_{\text{cut}} - |\mathbf{R}_j(t_0+\lambda'\delta\hat{\tau}) - \mathbf{R}_i(t_0+\lambda\delta\hat{\tau})|). \tag{34}$$

We first examine the effects of choosing a time correlation in terms of t_{cut} while setting R_{cut} such that the summation includes all events on the basis of their separation, using a 2× 2 ×2 supercell. For this case we find that choosing t_{cut} corresponding to the scaled time counter $\bar{s}_{\text{cut}}$= 2 hops/ion, results in a convergence parameter defined in Eq. (28) to be $\epsilon/|\langle \Delta^{\text{corr}}_{\text{cr}}(t_0,\tau)\rangle_{t_0}| \leq 1\%$. This result illustrates how the time correlation of "event products" differs from time convergence of cross-interaction

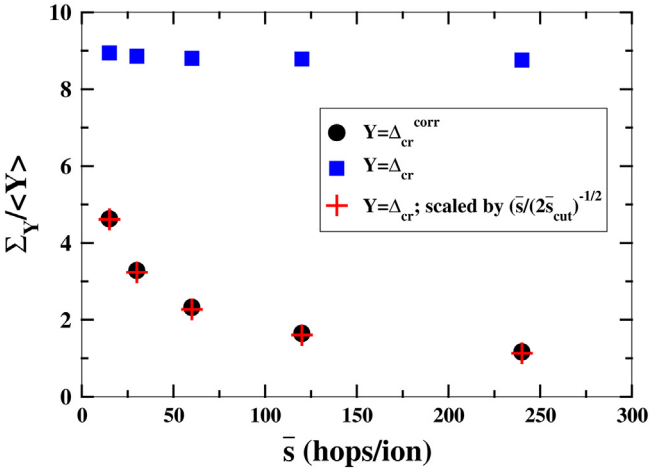

Fig. 11. Comparison of fractional standard deviations $\Sigma_Y/\langle Y\rangle$ for correlated and non-correlated evaluations of cross-interaction displacements evaluated for $2 \times 2 \times 2$ supercells. For $\langle \Delta_{cr}^{corr}(t_0, \tau)\rangle_{t_0}$, the time correlation was chosen corresponding to $\bar{s}_{cut}$= 2 hops/ion, while the spatial correlations were unrestricted. The plus symbols denote results derived from the full calculations of $\langle \Delta_{cr}(t_0, \tau)\rangle_{t_0}$ scaled as explained in the text.

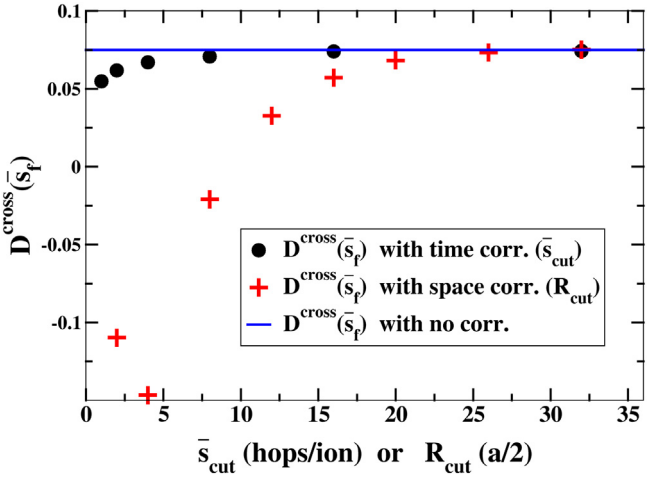

Fig. 12. Plots of $D^{cross}(\bar{s}_f)$ evaluated for a $80 \times 2 \times 2$ supercell for $\bar{s}_f = 62$ hops/ion. The blue line shows the value calculated using Eq. (8). The black circles show the results obtained from using Eq. (33) to calculate $\langle \Delta_{cr}^{corr}(t_0, \tau)\rangle_{t_0}$ with $\bar{s}_{cut}$ as indicated on the horizontal axis (in units of hops/ion) and no spatial correlation. The red crosses show the results obtained from using Eq. (33) to calculate $\langle \Delta_{cr}^{corr}(t_0, \tau)\rangle_{t_0}$ with R_{cut} as indicated on the horizontal axis (in units of a/2) and no time correlation.

diffusion. For this system, the interpolation model defined in Eq. (27) fits the simulation with $D_\infty = 0.054$ and $w = 0.344$. This means that any simulation which is well converged with respect to initial configurations carried out to a time interval equivalent to $\bar{s} = 2$ hops/ion, has an error of 16% relative to the time converged value because $D^{cross}(\bar{s} = 2)/D^{cross} = 0.84$. In order to reduce the convergence error to 1%, one needs to carry out the simulations out to a time interval equivalent to $\bar{s} = 34$ hops/ion. Nevertheless, in the formulation of the cross interaction diffusion in terms of event products as given in Eq. (33), we see that keeping only product pairs whose time differences are within t_{cut} corresponding to $\bar{s}_{cut} = 2$ hops/ion gives good results. To examine this further, we consider the fractional variances $\Sigma_Y/\langle Y\rangle$ for $\langle Y\rangle = \langle \Delta_{cr}(\bar{s})\rangle_{t_0}$ and $\langle \Delta_{cr}^{corr}(\bar{s})\rangle_{t_0}$ as shown in Fig. 11. Here we see that the fractional standard deviation computed using the correlated events converges toward zero while the fractional standard deviation computed using the full cross displacement asymptotes to constant value, consistent with the notion that keeping only the correlated events reduces the noise of the calculation. It is also interesting to note that an empirical scaling relationship between the fractional variance is found to be

$$\frac{\Sigma_{\Delta_{cr}^{coor}(\bar{s})}}{\langle \Delta_{cr}^{coor}(\bar{s})\rangle} \approx \frac{\Sigma_{\Delta_{cr}(\bar{s})}}{\langle \Delta_{cr}(\bar{s})\rangle} \frac{1}{\sqrt{\bar{s}/(2\bar{s}_{cut})}}, \tag{35}$$

where in this case $\bar{s}/(2\bar{s}_{cut})$ represents a multiplier for the data sampling made possible by including the correlated terms in Eq. (33) with t_{cut}. This scaling is shown in Fig. 11.

In investigating spatial correlations in evaluating Eq. (33), it was found that a large value of R_{cut} is needed to converge the cross interaction diffusion. For example, for cubic $n \times n \times n$ supercells, for all $1 \le n \le 16$, we found it necessary to include all events in the simulation according to their spatial separation in order to achieve converged results for Δ_{cr}^{corr}. Because the restricted sum in Eq. (33) for our model scales as $2n^6s^2$, it is computationally difficult to examine cubic simulation cells with $n > 16$. However, it is feasible to study the nature of the long spatial range correlations, within an asymmetric supercell. For example, we performed a series of simulations for the $80 \times 2 \times 2$ supercell system, separately studying the effects of time and space correlations. The results are presented in Fig. 12. For this system, we found that $D^{cross}(\bar{s}_f)/D^{cross}(\bar{s} \to \infty) = 95\%$ for $\bar{s}_f = 62$ hops/ion and that value was used in the evaluations presented in the figure. The results show that for this system the time correlation is well converged for $\bar{s}_{cut} \ge 8$ hops for ions, but the spatial correlation is only well converged at a distance of $R_{cut} \ge 20a/2$.

5.2. Statistical analysis of first principles simulations

The inspiration for this detailed study of the statistical properties of transport coefficients came from our recent first principles investigation [7] of the solid state electrolyte Li_2OHCl. In the disordered cubic phase of this material, the Li sublattice is the same as that shown in Fig. 1. While the first principles simulations are able to incorporate much more physically realistic interactions of the material into the simulations, the increased physical accuracy reduces the number of hops/ion that can be computed compared to the results obtained with the same computer resources using the kinetic Monte Carlo model. The hope is that our kinetic Monte Carlo simulations for this system can be used together with the first principles simulations to obtain a more complete understanding of its ionic diffusion. Of particular interest is the result suggested by comparing simulations for D^{tracer} with experimental results for the ionic conductivity using Eq. (13), that at experimentally accessible temperatures, the Haven ratio H_r for this system is greater than 1 and increases with decreasing temperature.

In the present work, we performed both first principles simulations and kinetic Monte Carlo simulations using $2 \times 2 \times 2$ supercells. Apart from using a smaller simulation cell in order to improve the computational statistics, the computational methods used for the first principles simulations were the same as those used in our previous work [7]. In particular, the first principles formalism is based on density functional theory (DFT) [24,25] implemented using the projector augmented wave (PAW) method [26] using the Quantum Espresso software package [27]. The calculational parameters were similar to those specified in the previous publication [7] except that the plane wave expansion of the wavefunctions included reciprocal lattice vectors $|\mathbf{k} + \mathbf{G}|^2 \le 35$ Ry and the wave vector sampling of the Brillouin zone included a $2 \times 2 \times 2$ grid.

For this study, twenty randomly generated configurations were prepared for $2 \times 2 \times 2$ supercells representing the disordered cubic phase of Li_2OHCl. The cubic lattice constant was fixed at $a = 3.91$ Å. The eight O and eight Cl positions were fixed at their ideal lattice positions. The 16 Li positions were randomly selected based on the unit cell shown in Fig. 1 and hydrogen locations were placed with the OH

bond length assumed to be 1.0 Å and a randomly chosen bond angle within all possible 4π radians. For each of the twenty initial structures, the static lattice internal energies were optimized at constant volume. Subsequently, first principles molecular dynamics simulations for these twenty optimized structures were performed at constant volume for two different target temperatures of $T = 750$ K and $T = 1000$ K. The simulations were performed in a microcanonical ensemble, at constant energy in terms of the kinetic energy associated with nuclear motion and electronic total DFT energy. The approximate simulation temperatures were controlled by initiating the calculations with velocity distributions corresponding to twice the target temperature values. While the first principles simulation times extended to $\tau = 180$–250 ps for the simulations at target temperature $T = 750$K and to $\tau = 90$–170 ps for the simulations at target temperature $T = 1000$K, it is clear that the results are not converged with respect to configuration averaging and with simulation time. Nevertheless, by pairing the first principles results with analogous kinetic Monte Carlo simulations, taking care to use equivalent levels of statistics, it is possible to make a statistically significant differentiation of the two models. In this case, the first principles simulations include, in addition to the realistic treatment of interparticle interactions, the effects of lattice vibrations, and a possible "gating" mechanism of the OH bond orientation. On the other hand, the kinetic Monte Carlo model includes only the geometric features of the Li sublattice.

In order to align the two calculations, we noted that for the kinetic Monte Carlo simulations, the parameter $\bar{s}$ represents the hops/ion. According to the extension of Eq. (7) for three-dimensional diffusion, the hops/ion can be estimated for a first principles simulation at a time duration τ according to

$$\bar{s}_\tau \approx \frac{\Delta_{sf}^x(t_0,\tau) + \Delta_{sf}^y(t_0,\tau) + \Delta_{sf}^z(t_0,\tau)}{N(a^2/2)}. \quad (36)$$

In this case $a^2/2$ approximates the three-dimensional hop length for this system, and $\bar{s}_\tau$ approximates the number of hops for the simulation time τ. It is reasonable to assume that the hop counter $\bar{s}_\tau$ determined from each first principles simulation run is analogous to the scaled hop counter $\bar{s}$ used in the Monte Carlo simulations. In this way, we could deduce that on average the two sets of temperature simulations corresponded to $\bar{s}$= 11 hops/ion and $\bar{s}$= 3.5 hops/ion for the 1000 K and 750 K simulations respectively. The corresponding ranges of $\bar{s}$ were 4.75–21.25 and 1.5–5.6, respectively. In order to improve the statistical sampling, each of the first principles simulations was analyzed separately, averaging the results for the entire runs into $\bar{s} = 1$ hop/ion segments and determining the average temperature of each run. Correspondingly, for both the $T = 1000$ K and $T = 750$ K temperature ranges, sets of 20 Monte Carlo simulations were performed using similar sampling statistics. That is for each Monte Carlo run, the total simulation was fixed at $\bar{s}$= 11 (3.5) hops/ion for the $T = 1000$ K (750 K) cases and the results for the entire run was averaged by analyzing $\bar{s} = 1$ hop/ion segments. While physical temperature effects are not explicitly included in the Monte Carlo runs, their effects on the statistical sampling were modeled as closely as possible in this way. The results were analyzed in terms of the Haven ratios, calculated from Eq. (12) at finite simulation time corresponding to $\bar{s}$= 1 hop/ion and the results are presented in Fig. 13.

The results for H_r shown in Fig. 13 show substantial statistical noise as well as systematic error, however a clear distinction of the behavior of ion diffusion in the realistic "first principles" model relative to that of the kinetic Monte Carlo results is demonstrated. Knowledge of systematic errors comes from the Monte Carlo studies for which it was shown previously that at this level of statistical time, the simulations were still not at their asymptotic limit. The value of the Haven ratio from the Monte Carlo model for a $2\times 2\times 2$ supercell converged with time intervals of $\bar{s}$=1 hop/ion is $H_r \approx 0.92$, while the converged value is $H_r = 0.84$. Nevertheless, the results for the first principles simulations suggest that $H_r > 1$ in the temperature range of $T = 750$ K and

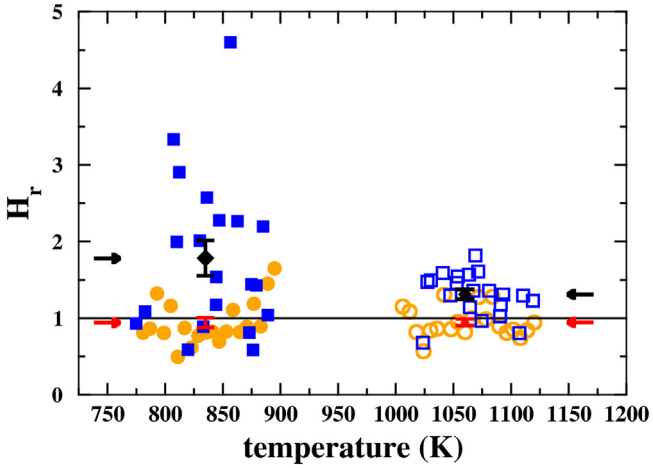

Fig. 13. Results of combined first principles and Monte Carlo study of the Haven ratio for the disordered cubic phase of Li_2OHCl simulated at a target temperature of 750 K (filled symbols) and a target temperature of 1000 K (open symbols). For each target temperature, the blue symbols indicate the first principles results calculated for 20 initial configurations at the indicated average temperatures. The orange symbols indicate the Monte Carlo results calculated for 20 initial configurations with comparable statistics to the first principles runs as explained in the text. For the Monte Carlo results the horizontal axis placement is arbitrarily assigned for visualization. The averaged first principles results are indicated with black symbols and standard deviation of the mean error bars. The averaged Monte Carlo results are indicated with red symbols and standard deviation of the mean error bars. The black and red arrows highlight the averaged first principles and Monte Carlo values of H_r.

$T = 1000$ K and also suggest a temperature dependence of H_r such that $H_r(750\text{ K}) > H_r(1000\text{ K})$. The simulations at $T = 750$ and 1000 K were performed in order to improve the statistics, but in reality the material is not expected to exist in its crystalline form at such high temperatures. In our previous work [7], the suggestion was made that H_r is significantly larger than 1 in the temperature range of $315 < T < 470$ K based on simulations with inferior statistics and comparing to experimental conductivity measurements at those temperatures.

It is also interesting to consider possible mechanisms that cause $H_r > 1$ for this system. A possible physical mechanism comes from observing the short time behavior of $D^{cross}(\tau)$ which is shown in Fig. 14. In Fig. 14, the value of $D^{cross}(\tau)$ is shown for a simulation with average temperature 1074 K simulated to 140 ps and final value of Δ_{sf}/

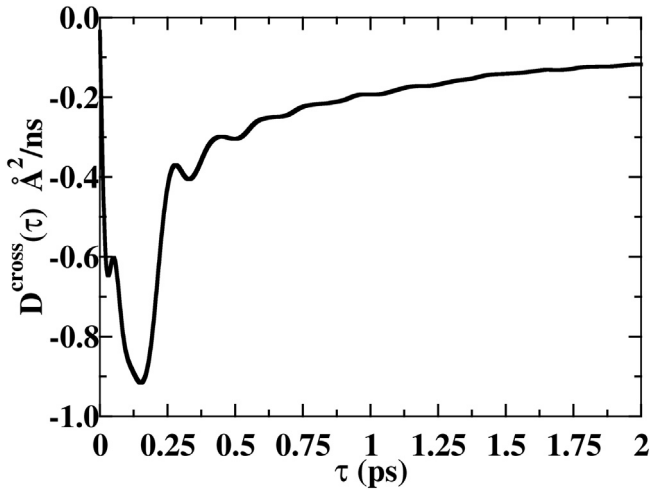

Fig. 14. Results of first-principles molecular dynamics simulation of $2\times 2\times 2$ supercell of Li_2OHCl at a temperature of $T = 1074K$ to determine $D^{cross}(\tau)$ for $0 \le \tau \le 2$ ps.

$N = 89\text{Å}^2$. In this calculation, the averaging over initial configurations was achieved by averaging the full simulations in terms of $\tau = 7$ps segments; the first 2 ps of the resultant $D^{\text{cross}}(\tau)$ are presented. It is interesting that $D^{\text{cross}}(\tau) < 0$ throughout this time range and that within the first 0.2 ps there is a negative dip indicating that the short time motions (vibrations) of the lithium atoms are anti-correlated. It can be argued that this anti-correlated property of the short time motion of the lithium ions contributes to the net bias for anti-correlated hopping which leads to a Haven ratio greater than 1.

6. Summary and conclusions

The results of this study both provide insight into the transport properties of a specific system, the disordered cubic phase of Li_2OHCl, and also provide detailed analysis of the statistical and convergence properties of transport simulations more generally. The work in this paper was motivated by the challenge of reaching the large statistical time scales (hops/ion) necessary to study these convergence properties. With the help of a lattice kinetic Monte Carlo model, it is possible to explore aspects of the transport simulations which rely on long simulation times, large simulation cells, and sampling over large numbers of initial configurations. For the Li_2OHCl system, we have been able to use the lattice kinetic Monte Carlo model together with first principles simulations to improve the prediction of the ionic correlations. While the lattice kinetic Monte Carlo model used in this work was based on the Li sublattice of the disordered cubic phase of Li_2OHCl, we expect that the qualitative statistical and convergence properties of the results can be generalized to other lattices.

In this work, we considered both transport coefficients calculated in the absence and presence of an applied electric field. Evaluated for a fixed supercell and fixed simulation time, the distribution of values obtained for different initial configurations was determined. We found that the distributions for $\Delta_{\text{sf}}(t_0, \bar{s})/2N\bar{s}$ and correspondingly $\mu_x(t_0, \bar{s})$ have a Gaussian shape and standard deviation that approaches zero in the limit of large sample size as represented by large supercells in the periodic boundary formulation. By contrast, the distribution of values of $\Delta_{\text{cr}}(t_0, \bar{s})/2N\bar{s}$ is found to have a very asymmetric distribution with a standard deviation that limits to a non-zero constant in the large supercell limit. The ratio of the standard deviation to mean value is found to limit to a non-zero constant in time for both the Δ_{sf} and Δ_{cr} terms. However, the ratio of the standard deviation to mean value of μ_x tends to zero in the long time limit at a rate that depends on the applied field strength used in the calculations. The statistical results indicate that for the Kubo formalism, the primary difficulty of convergence is due to the Δ_{cr} term which requires a large number of initial configurations. For the Ohm's law formulation of the transport simulations, the statistical results indicate that calculation of ionic conductivity would benefit from use of a field strength adjusted to the largest magnitude possible while still remaining in the linear response regime. Adapting the Ohm's law formulation to first principles simulations would need additional considerations.

The lattice kinetic Monte Carlo simulations also were used to assess the convergence of the transport parameters with respect to simulation time and system size given high convergence with respect to initial configurations. In terms of supercell size, the results show that for this lattice geometry the properties of interest are well converged for a cubic supercell composed of $6 \times 6 \times 6$ unit cells. In terms of simulation time, the results for cubic supercells, both $D^{\text{tracer}}(\bar{s})$ and $D^{\text{cross}}(\bar{s})$ can be represented by a simple interpolation form from which the asymptotic form can be determined. For the lattice considered in this work, $D^{\text{effective}}(\bar{s})$ converged at very short time. It is not clear whether or not this feature is more generally true for other lattice geometries.

This work also introduces an alternate formulation of Δ_{cr} in terms of a sum over event products for the purpose of considering temporal and/or spatial correlations. For an example system, we found that including only event pairs separated in time by $\bar{s}_{\text{cut}} = 2$ hops/ion or less in the calculation of $\Delta_{\text{cr}}^{\text{corr}}$ reduced the fractional standard deviation substantially. This suggests that, for long simulations, restricting the sum over event products in time can be used to reduce the noise in the calculation and therefore improve the calculational efficiency. Translating this idea into a practical computational scheme is not trivial, since it is generally difficult to estimate $\bar{s}_{\text{cut}}$, but probably worth further consideration. This study also showed that spatial correlations in this system are long range.

The lattice kinetic Monte Carlo simulations were used to closely analyze the statistics of analogous first principles simulations of $\Delta_{\text{cr}}(t_0,\tau)$ the full Li_2OHCl lattice. We were able to improve the statistical analysis to provide further evidence about the Haven ratio, showing that $H_r > 1$ at the simulation temperatures. Interestingly, a plot of $D^{\text{cross}}(\tau)$ from the first principles simulations, shows negative values for $0 \le \tau \le 2$ ps with a negative peak at approximately $\tau = 0.2$ ps. This time generally corresponds to vibrational modes in the lattice and suggests that these vibrations may lead to short time anti-correlated motions. The first principles result for $D^{\text{cross}}(\tau)$ shown in Fig. 14 can be contrasted with the corresponding result for the lattice kinetic Monte Carlo model which has a shape similar to that shown in Fig. 10, monotonically increasing above zero. This example shows how the lattice kinetic Monte Carlo simulations can be used to estimate the level of statistics necessary to converge the more accurate simulations of the transport parameters. The lattice kinetic Monte Carlo results for the transport parameters can also serve as a well defined reference which captures the geometric and site blocking effects.

Acknowledgments

This work was supported by the National Science Foundation of the United States of America grant DMR-1507942. Computations were performed on the Wake Forest University DEAC cluster, a centrally managed resource with support provided in part by the University.

References

[1] N. Kamaya, K. Homma, Y. Yamakawa, M. Hirayama, R. Kanno, M. Yonemura, T. Kamiyama, Y. Kato, S. Hama, K. Kawamoto, A. Mitsui, Nat. Mater. 10 (2011) 682.
[2] D. Zahn, J. Mol. Model. 17 (2011) 1531.
[3] Y. Mo, S.P. Ong, G. Ceder, Chem. Mater. 24 (2012) 15.
[4] Z.D. Hood, H. Wang, A. Samuthira Pandian, J.K. Keum, C. Liang, J. Am. Chem. Soc. 138 (2016) 1768.
[5] Y. Li, W. Zhou, S. Xin, S. Li, J. Zhu, X. Lü, Z. Cui, Q. Jia, J. Zhou, Y. Zhao, J.B. Goodenough, Angew. Chem. Int. Ed. 55 (2016) 9965.
[6] G. Schwering, A. Hönnerscheid, L. van Wüllen, M. Jansen, ChemPhysChem 4 (2003) 343.
[7] J. Howard, Z.D. Hood, N.A.W. Holzwarth, Phys. Rev. Mater. 1 (2017) 075406.
[8] A.-Y. Song, Y. Xiao, K. Turcheniuk, P. Upadhya, A. Ramanujapuram, J. Benson, A. Magasinski, M. Olguin, L. Meda, O. Borodin, G. Yushin, Adv. Energy Mater. 8 (2018) 1700971.
[9] K. Campaan, Y. Haven, Trans. Faraday Soc. 54 (1958) 1498.
[10] Y. Haven, B. Verkerk, Phys. Chem. Glasses 6 (1965) 38.
[11] A.D. Le Claire, Correlation effects in diffusion in solids, in: W. Jost (Ed.), Physical Chemistry An Advanced Treatise, vol. X/Solid State, Academic Press, New York, 1970, pp. 261–330 Chap. 5.
[12] G. Murch, Solid State Ionics 7 (1982) 177.
[13] A. Marcolongo, N. Marzari, Phys. Rev. Mater. 1 (2017) 025402.
[14] X. He, Y. Zhu, Y. Mo, Nat. Commun. 8 (2017) 15893.
[15] A. Van der Ven, G. Ceder, M. Asta, P.D. Tepesch, Phys. Rev. B 64 (2001) 184307.
[16] R. Kubo, J. Phys. Soc. Jpn. 12 (1957) 570.
[17] J.M. Haile, Molecular Dynamics Simulation: Elementary Methods, John Wiley & Sons, Inc., 1992 ISBN: 978-0-471-81439-3.
[18] N. Kuwata, X. Lu, T. Miyazaki, Y. Iwai, T. Tanabe, J. Kawamura, Solid State Ionics 294 (2016) 59.
[19] N. Metropolis, A.W. Rosenbluth, M.N. Rosenbluth, A.H. Teller, E. Teller, J. Chem. Phys. 21 (1953) 1087.
[20] J. Manning, Diffusion Kinetics for Atoms in Crystals, Van Nostrand, 1968.
[21] S. Ihara, K. Suzuki, J. Phys. Soc. Jpn. 55 (1986) 1695.

[22] In principle, following the work of Van der Ven et al. [15], a more sophistocated kinetic Monte Carlo model could be used with configuration dependent activation energies. However, in this work, the representation of the important effects of the rotating OH groups within such a scheme is intractable.
[23] P.R. Bevington, Data Reduction and Error Analysis for the Physical Sciences, McGraw-Hill Book Company, 1969.
[24] P. Hohenberg, W. Kohn, Phys. Rev. 136 (1964) B864.
[25] W. Kohn, L.J. Sham, Phys. Rev. 140 (1965) A1133.
[26] P.E. Blöchl, Phys. Rev. B 50 (1994) 17953.
[27] P. Giannozzi, O. Andreussi, T. Brumme, O. Bunau, M.B. Nardelli, M. Calandra, R. Car, C. Cavazzoni, D. Ceresoli, M. Cococcioni, N. Colonna, I. Carnimeo, A.D. Corso, S. de Gironcoli, P. Delugas, R.A. DiStasio Jr, A. Ferretti, A. Floris, G. Fratesi, G. Fugallo, R. Gebauer, U. Gerstmann, F. Giustino, T. Gorni, J. Jia, M. Kawamura, H.-Y. Ko, A. Kokalj, E. Kkbenli, M. Lazzeri, M. Marsili, N. Marzari, F. Mauri, N.L. Nguyen, H.-V. Nguyen, A.O. de-la Roza, L. Paulatto, S. Ponc, D. Rocca, R. Sabatini, B. Santra, M. Schlipf, A.P. Seitsonen, A. Smogunov, I. Timrov, T. Thonhauser, P. Umari, N. Vast, X. Wu, S. Baroni, J. Phys. Condens. Matter 29 (2017) 465901.